université

PARIS-SACLAY

Thèse de doctorat

Search of the $0\nu\beta\beta$ decay with the SuperNEMO demonstrator

Thèse de doctorat de l'Université Paris-Saclay
préparée à l'Université Paris Saclay au sein du Laboratoire Irène-Joliot Curie
(anciennement Laboratoire de l'Accélérateur Linéaire)

École doctorale n°576 Particles, Hadrons, Energy, Nuclei, Instrumentation,
Imaging, Cosmos et Simulation (PHENIICS)
Spécialité de doctorat : Physique des particules

Thèse présentée et soutenue à Orsay, le ***, par

CLOÉ GIRARD-CARILLO

Composition du Jury :

***
***   Président

***
***   Rapporteur

***
***   Rapporteur

Christine Marquet
CENBG - Bordeaux-Gradignan   Examinateur

***
***   Examinateur

***
***   Examinateur

Laurent Simard
LAL - Orsay   Directeur de thèse

Mathieu Bongrand
LAL - Orsay   Co-directeur de thèse

Contents

Sensitivity of the SuperNEMO demonstrator to the $0\nu\beta\beta$

In this chapter, we present a study aiming to evaluate the SuperNEMO's sensitivity to the $0\nu\beta\beta$ decay, and the corresponding effective neutrino mass. Studies of this kind have already been conducted, and the final detector, based on the NEMO-3 technology, is expected to exclude half-lives up to 1.2×10^{26} y (90% CL), with an exposure of 500 kg.y for the ^{82}Se[1] [8]. In order to assess the feasibility of such a large-scale detector, the SuperNEMO demonstrator started to be installed in early 2015, at the Laboratoire Souterrain de Modane. With an exposure of 17.5 kg.y, this demonstrator could reach a sensitivity on the $0\nu\beta\beta$ process of 5.3×10^{24} y (90% CL) [9].

At the time of the current analysis, the coil, which is supposed to deliver a magnetic field inside the detector, was not yet installed on the demonstrator. We aim to explore the impact, on both the demonstrator and final detector sensitivity, of the presence of this magnetic field. The findings of this study will participate in the final decision on the installation of the coil. In a context of investigating the demonstrator and final detector's capabilities, different internal source contamination levels are considered. The topology of interest is the two electrons topology, and we use the total energy sum to discriminate the signal from the background events. Thanks to SuperNEMO tracking capabilities, topological informations are exploited to improve the sensitivity. To go further, we are also exploring the possibility of studying the $0\nu\beta\beta$ decay of another isotope, ^{150}Nd.

7.1 The $0\nu\beta\beta$ Signal and background model

A full simulation for the demonstrator was performed, in order to determine the upper limit on $0\nu\beta\beta$ half-life that can be probed with SuperNEMO. This sensitivity greatly depends on the number of detected but non-rejected background events.

Due to the time it would take to simulate every expected background contribution, the choice of a simplified background model, containing only the most harmful backgrounds to the $0\nu\beta\beta$ decay search, was adopted. These backgrounds

---

[1]Supposing Selenium-82 $0\nu\beta\beta$ decays through the exchange of a light Majorana neutrino.

are the $2\nu\beta\beta$ decay, a contamination of the source in ^{208}Tl and ^{214}Bi, and a contamination of the tracker gas with Radon. The number of natural isotope decay events expected depends on their activities inside the source foils (for Thallium-208 and Bismuth-214), or on the tracker's wires (for Radon-222 decaying in Bismuth-214). It was necessary, during the design of the detector, to constrain the maximal tolerable activities, to guarantee a high sensitivity to the $0\nu\beta\beta$ disintegration [10]. The collaboration then established recommendations for maximum levels of internal background, given in number of disintegrations per second, for a unit mass of $\beta\beta$ isotope, or for a unit volume of gas. These are the so-called specified activities. The amount of expected double β decays is driven by its half-life value: the higher the half-life, the lower its contribution in the total number of expected background. For Selenium-82 sources, we take the $2\nu\beta\beta$ half-life measured by NEMO-3, $T_{1/2}^{2\nu} = 9.39 \pm 0.17$ (stat) ± 0.58 (syst) $\times 10^{19}$ years [11]. Moreover, we choose to consider the best limit set on the $0\nu\beta\beta$ process, of $T_{1/2}^{0\nu} > 2.5 \times 10^{23}$ y [11]. In the Tab. 7.1 is summarised the expected number of signal and background events, per disintegration unit per second, for one kg of source material, or for one m^3 of gas inside the tracker. These figures are presented both for the

Type of decay	Expected decays		Simulated decays
	Demonstrator	Final detector	
$0\nu\beta\beta$ ($T_{1/2}^{0\nu} = 2.5 \times 10^{23}$ y)	$3.6\,10^2$	$1.0\,10^4$	$1.0\,10^7$
$2\nu\beta\beta$ ($T_{1/2}^{2\nu} = 9.39 \times 10^{19}$ y)	$9.5\,10^5$	$2.7\,10^7$	$1.0\,10^7$
^{208}Tl ($\mathcal{A}^{\text{Tl}} = 10\,\mu$Bq/kg)	$5.5\,10^3$	$1.6\,10^5$	$1.0\,10^7$
^{214}Bi ($\mathcal{A}^{\text{Bi}} = 2\,\mu$Bq/kg)	$1.1\,10^3$	$3.1\,10^4$	$1.0\,10^7$
^{222}Rn ($\mathcal{A}^{\text{Rn}} = 0.15$ mBq/m^3)	$1.8\,10^5$	$7.2\,10^6$	$1.0\,10^8$

Table 7.1: Expected and simulated decays for different processes, both for the demonstrator (17.5 kg.y) and for the final detector exposures (500 kg.y), assuming target background activities are reached: $\mathcal{A}^{\text{Tl}} = 10\,\mu$Bq/kg, $\mathcal{A}^{\text{Bi}} = 2\,\mu$Bq/kg, $\mathcal{A}^{\text{Rn}} = 0.15$ mBq/m^3. The measured half-life $T_{1/2}^{2\nu} = 9.39 \times 10^{19}$ y for Selenium-82's $2\nu\beta\beta$ is taken, and we assume $T_{1/2}^{0\nu} = 2.5 \times 10^{23}$ y [11].

SuperNEMO demonstrator and final detector. They represent the total number of disintegrations, without taking into account any technique to reject background, and for the total energy window. Nevertheless, the number of decays presented in this table are expected to be extremely reduced, notably by the application of event selections aimed at maximising the sensitivity to the excluded $0\nu\beta\beta$ half-life (Sec. 7.2). This effect is augmented by the fact that, for the current sensitivity analysis, we focus on a narrow energy window, called *region of interest*, whose usefulness is described in more detail in Sec. 7.2. Therefore, to properly conduct this sensitivity study, it was necessary to simulate a large number of events, so that the signal and backgrounds are correctly represented in the region of interest. In the table are presented the amount of events we simulated for each process listed.

7.1.1 The $0\nu\beta\beta$ signal

The SuperNEMO detector was designed to search for the never-observed $0\nu\beta\beta$ decay. In the following, we assume the underlying mechanism for this decay is the exchange of a light Majorana neutrino, the so-called mass mechanism (MM), as it is the most widespread mechanism. The hypothetical $0\nu\beta\beta$ signal would be detected as an excess of events in the region of interest, with respect to the predicted background contamination levels. Some 10^7 $0\nu\beta\beta$ events were simulated inside the source foils, using the DECAY0 software [12]. The simulations are normalised assuming the half-life excluded by NEMO-3, $T_{1/2}^{0\nu} > 2.5 \times 10^{23}$ y (90% CL) [11].

7.1.2 Inside detector backgrounds

In addition with the $0\nu\beta\beta$ decay, we simulated different types of backgrounds, that could mimic the searched signal.

7.1.2.1 Internal backgrounds

The so-called *internal backgrounds* stand for decays occurring inside the source foils, presenting the same signature as the $0\nu\beta\beta$ signal. These backgrounds, already introduced earlier, are the $2\nu\beta\beta$ of the source isotope, as well as disintegrations of ^{208}Tl and ^{214}Bi inside the source foils.

The $2\nu\beta\beta$ process

In the full energy range, the allowed $2\nu\beta\beta$ decay stands as the dominant internal background type. Its total energy spectrum is a continuum, whose ending point should stands at $Q_{\beta\beta} = 2.99$ MeV, but is slightly shifted by the detector's energy resolution. We simulated 10^7 events of this decay inside the source foils, in the full energy window. However, above a certain energy value, the number of $2\nu\beta\beta$ events decreases very quickly. To offset this effect, we simulated additional 10^7 of this decay on a slightly lower energy range, that is to say above 2 MeV. The second set of simulations is normalised with the first one. In this way, the lack of $2\nu\beta\beta$ simulated events in the high-energy tail is avoided, without requiring too high computational resources.

Source foils contamination by natural isotopes

As described in Sec. 3.2.1, after sources purification, remaining natural isotopes such as ^{208}Tl or ^{214}Bi can still be present inside the foils. This class of contamination constitutes the principal internal source of background, with the $2\nu\beta\beta$ decay. We simulated 10^7 decays both for the two isotopes, inside the source foils.

7.1.2.2 Tracker contamination by natural isotopes

The presence of gaseous Radon-222 inside the tracker, mainly deposited on the copper wires, can produce events similar to internal one. In fact, one of the progeny

of Radon-222, the Bismuth-214, can decay on (or near) a foil, and appear with a two-electron ($2e$) topology, becoming hard to distinguish from a double beta decay candidate. As this isotope is distributed throughout the whole tracking detection volume, to study the experiment's sensitivity, we simulated a large quantity of this decay, that is to say 10^8 decays on the tracker wires.

7.1.3   External backgrounds

This background category is populated by the external γ-ray flux produced by radioactive isotope decays in detector components or surrounding laboratory rocks, as well as neutron interactions in the external iron shield. As external background simulations would be very consumming in terms of computing ressources, it is important to ensure that they are necessary. The NEMO-3 experiment set a limit on the external background number of counts, of < 0.2 events in the $2e$ topology, for the energy range [2.8;3.2] MeV (two electrons energy sum), for an exposure of 34.3 kg·y, with ^{100}Mo sources [14]. Radiopurity measurements of the SuperNEMO PMTs allow to conclude that the total ^{214}Bi activity is 35% better than for those of NEMO-3 [13], which is encouraging. Unfortunately, these measurements also revealed that the total budget in ^{208}Tl isotope is 150% higher than NEMO-3. This could lead us to think that the external background for SuperNEMO could be higher than that of NEMO-3. However, on that level, the most notorious difference between the two detectors is the fact that the SuperNEMO scintillator blocks are thicker than those of NEMO-3. Therefore, a gamma is more likely to be detected and, in that case, the event would not contribute to the background in the $2e$ channel. Even if the regions of interest are slightly different between these two experiments, it produces negligible increase on the external background contribution[2]. After all, given the fact that SuperNEMO is expected to be better than NEMO-3 at rejecting external background events, we consider that all external backgrounds from outside the foil, apart from ^{222}Rn in the tracking volume, are expected to be negligible, and were not simulated.

7.2   Event selection

For SuperNEMO, the $0\nu\beta\beta$ signature is two-electrons events, emitted simultaneously from the same vertex on the source foils, with an energy sum compatible with $Q_{\beta\beta} = 2.99$ MeV for the Selenium-82. Therefore, we conducted this analysis selecting only events matching the $2e$ topology, where a reconstructed particle is tagged as an electron if it has

- a vertex on the source foils,

- a reconstructed track inside the wire chamber,

---

[2]A study conducted by the SuperNEMO collaboration shown that only 0.73 additional external background events would have been expected for the NEMO-3 detector, if instead of taking the [2.8;3.2] MeV energy range, we would have considered the [2.7;3.15] MeV region of interest.

- an associated calorimeter hit,

- and a final criterion depending on the case under consideration. In fact, as announced, this study also aims at considering two separate magnetic field cases. One where the magnetic field has a value of 25 Gauss along the Z (vertical) axis of the detector, and one where the field is turned off. In the first case, particles such as electrons and positrons of a few MeV have a curved trajectory in the tracker. In the second case, the tracks of the particles may be similar to straight lines (not to mention the possible multiple scattering on the wires of the tracker). It is then necessary to adapt the selection of events to each case. We then consider an additional criterion: a particle is identified as an electron if its track has a negative curvature. In the following, we present results where the magnetic field is turned on. The off-field study is addressed in Sec. 7.5.

All these selections represent the so-called *first-order* cut-offs. We present the total energy spectra for each simulated process, after application of these cut-offs, in Fig. 7.1. We present results for the specific case were of the demonstrator (Selenium-82 sources, 17.5 kg/y exposure), with the specified internal contamination levels ($\mathcal{A}^{\mathrm{Tl}} = 10\,\mu\mathrm{Bq/kg}$ and $\mathcal{A}^{\mathrm{Bi}} = 2\,\mu\mathrm{Bq/kg}$).

The $0\nu\beta\beta$ distribution is expected as a peak at the end-point of the $2\nu\beta\beta$ energy distribution. Nervertheless, we observe the spectrum is asymmetric, and peaked around 2.8 MeV. Indeed, the measurement of the available energy $Q_{\beta\beta} = 2.99$ MeV is degraded by electron energy losses, before reaching the calorimeter (mainly inside the dense source material, as well as inside the wire chamber), as well as by the calorimeter energy resolution. Concerning the $2\nu\beta\beta$ energy spectrum, we only present the events simulated with an energy > 2 MeV, even if all simulated events were taken into account for this study. Whatever their origin, either Radon-222 contaminations inside the tracker gas, or internal contaminations of the source foils, the two Bismuth-214 energy distributions have nearly the same shapes. The ^{208}Tl spectrum reveals the internal conversion of the 2.614 MeV gamma, emitted after ^{208}Tl β^- disintegrations. All spectra are normalised to the natural isotopes specified activities, and the half-lifes values.

A widespread technique consists in constraining the $0\nu\beta\beta$ decay searches to a narrow energy range, the so-called *region of interest* (ROI), materialised by the two vertical dashed lines in the figure. In the following, we expose general principles leading to the determination of the best limit on $T^{0\nu}_{1/2}$, in the appropriate region of interest. We illustrate the reasoning with the demonstrator, specified activities, on-magnetic field case. However, the technique presented remain valid for all exposures, internal contamination levels and field conditions. The impact of all these parameters is detailed in the rest of the chapter.
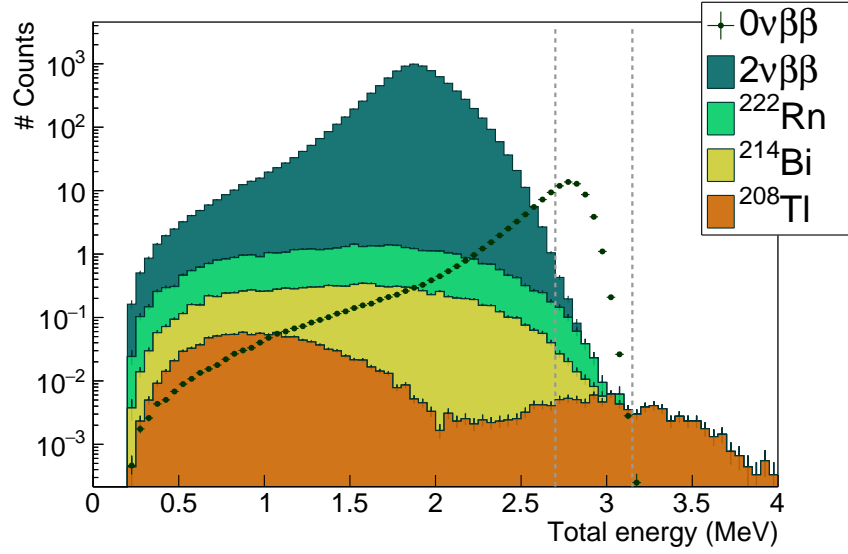
(a)
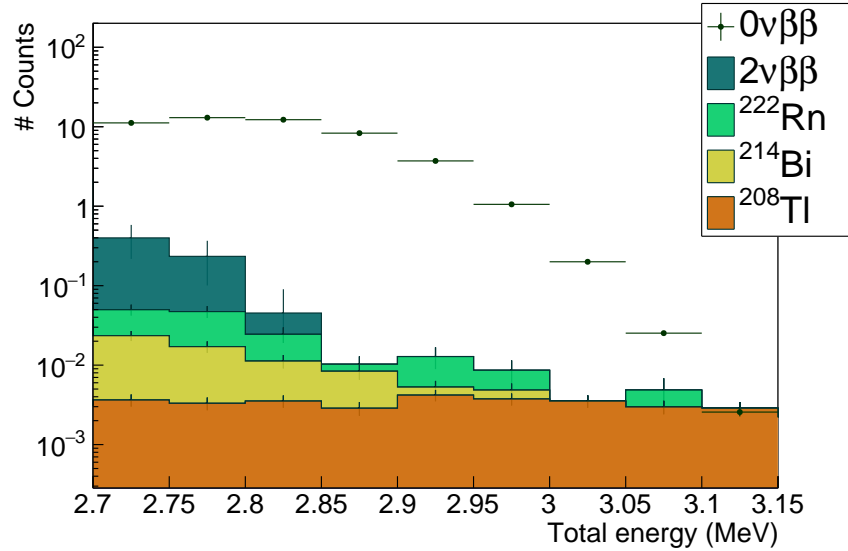
(b)

Figure 7.1: Total energy spectra for the $0\nu\beta\beta$ signal and main backgrounds, for (a) the full energy range, and (b) for the [2.7;3.15] MeV energy range, whose optimisation is discussed in Sec. 7.3.

7.3   Demonstrator sensitivity to the Selenium-82 $0\nu\beta\beta$ decay

In case of the non-observation of a $0\nu\beta\beta$ signal, the expected upper limit on the half-life is provided for a given $[E_{\min};E_{\max}]$ energy range, and depends on the characteristics of the detector. First, it depends on the signal detection efficiency $\epsilon_{0\nu}$ in this energy window, secondly on the source isotope nature, as well as the

detector's exposure $m \times t$. It follows

$$T_{1/2}^{0\nu} > \frac{\mathcal{N}_A \ln 2}{M} \times \frac{\epsilon_{0\nu} \times m \times t}{N_{0\nu}^{\text{excl.}}}, \tag{7.1}$$

with $\mathcal{N}_A$ the Avogadro number, m the quantity of isotope in the source foils, M its molar mass, and t the total time of data taking. $N_{0\nu}^{\text{excl.}}$ is the number of signal events excluded, calculated with the Feldman-Cousins statistics from the total expected number of background events. The Feldman-Cousins statistics [16] is a wide-used method in rare events search experiments, providing confidence intervals for upper limits in the case of Poisson processes with background. We use this method in the framework of this analysis to provide a limit, at 90% CL, on the number of expected signal events $N_{0\nu}^{\text{excl.}}$, on the basis of the expected number of background events, given below.

- The $2\nu\beta\beta$ background
  In Eq. (7.1), we defined the upper limit on $T_{1/2}^{0\nu}$ from the number of excluded signal events, and the signal selection efficiency $\epsilon_{0\nu}$. The same way, we can define the number of expected $2\nu\beta\beta$ events, $N_{2\nu}$, from the half-life $T_{1/2}^{2\nu}$ and the $2\nu\beta\beta$ selection efficiency, $\epsilon_{2\nu}$, as

$$N_{2\nu} = \frac{\mathcal{N}_A \ln 2}{M} \times \frac{\epsilon_{2\nu} \times m \times t}{T_{1/2}^{2\nu}}. \tag{7.2}$$

- Natural radioactive backgrounds
  We consider the background massic activities $A_{\text{rad.}}$, and $\epsilon_{\text{rad.}}$ their selection efficiencies in a given energy window. The number of background events is therefore given, for the ^{208}Tl and ^{214}Bi internal contaminations, as

$$N_{\text{rad.}} = A_{\text{rad.}}\epsilon_{\text{rad.}} \times m \times t \tag{7.3}$$

where $A_{\text{rad.}}$ is given in Bq/kg. Similarly, for the ^{222}Rn background,

$$N_{\text{rad.}} = A_{\text{rad.}}\epsilon_{\text{rad.}} \times V \times t, \tag{7.4}$$

with $V = 15.3$ m^3 the tracker volume, and where $A_{\text{rad.}}$ represents this time a volumic activity, given in Bq/m^3.

All these equations, similarly as Eq. (7.1), are valid for a given energy range $[E_{\min}; E_{\max}]$. To find the optimal energy interval for the search of the $0\nu\beta\beta$ decay, that is to say the one maximising the limit on $T_{1/2}^{0\nu}$, we must vary the $E_{\min}$ and $E_{\max}$ bounds.

As can be seen in Fig. 7.1, beyond a certain value in energy, the number of background events becomes negligible. Indeed, the ^{208}Tl background dominates at these energies, where it do not exceed one count for E> 3.2 MeV. This is why the upper limit $E_{\max}$ of the energy interval has only a limited impact on the search for the best ROI. It is then natural to study mainly the influence of the lower limit $E_{\min}$. Therefore, the selection efficiencies, entering in the calculation of the $T_{1/2}^{0\nu}$ upper limit, are presented in Fig. 7.2, as a function of E $> E_{\min}$. We remind a
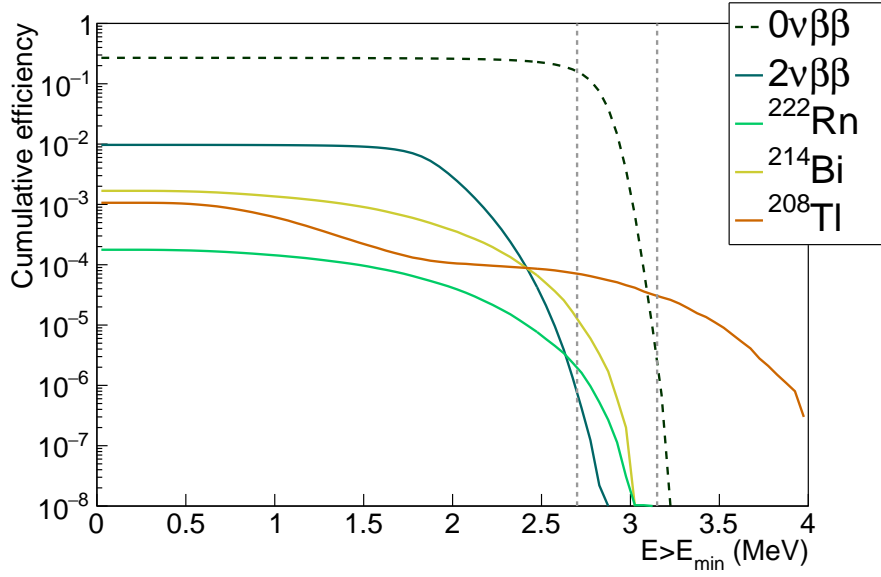
Figure 7.2: Efficiency spectra as a function of $E > E_{min}$, for the $0\nu\beta\beta$ signal (dashed black line) and for the main backgrounds (plain lines). The two vertical grey lines represent the final ROI optimised for the case of the demonstrator, taken the specified isotope activities.

selection efficiency ϵ is the ratio of the number of selected events, to the number of simulated events. As a matter of fact, we look for an energy region where $\epsilon_{0\nu}$ is high, and where selection efficiencies for the background are low. This choice directly determines the best value for $T_{1/2}^{0\nu}$ (90% CL), whose variation as a function of E_{min} and E_{max} are presented in Fig. 7.3. As we said, the energy range chosen as the region of interest for the search of the $0\nu\beta\beta$ decays is the one maximising the $T_{1/2}^{0\nu}$. We found that, for the demonstrator exposure, with ^{82}Se sources, with a 25 G magnetic field, and for the specified background activities, the best ROI is [2.7;3.15] MeV. In this optimised energy range, the sensitivity expected for the SuperNEMO demonstrator stands at

$$T_{1/2}^{0\nu} > 5.68 \times 10^{24}\,\text{y} \qquad (90\%\text{CL})\,. \tag{7.5}$$

This result is compatible with the previous analysis lead by Steven Calvez [9].

In this section, we presented the general procedure leading to an optimised result on the $T_{1/2}^{0\nu}$ limit, and we gave the best limit on $T_{1/2}^{0\nu}$, driven by Eq. (7.1), for the demonstrator case. Thereafter, we discuss the results obtained for different detector exposures (demonstrator and final detector), and different internal background activities. Also, and this is the main purpose of this study, we discuss the influence of the presence of the magnetic field on the final detector's sensitivity.
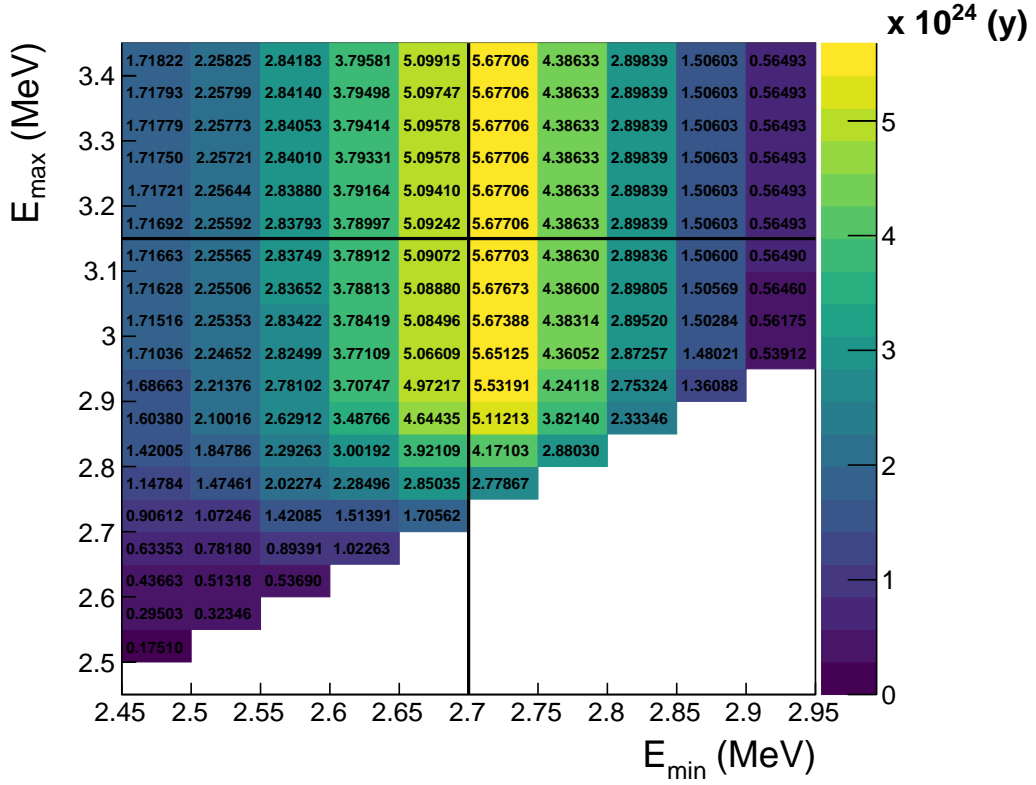
Figure 7.3: Two-dimensional histogram showing the evolution of the $T_{1/2}^{0\nu}$ value as a function of the lower and upper energy bounds. The maximal upper limit of $T_{1/2}^{0\nu} > 5.68 \times 10^{24}$ y (90% CL) is retained, in the [2.7;3.15] MeV region of interest.

7.4 Impact of sources contamination levels on the sensitivity

We study the impact of the isotope contamination levels (inside the source foils, as well as on the tracker's wires) on the $0\nu\beta\beta$ sensitivity. We also optimise additional event selections aimed at improving the final sensitivity result.

7.4.1 Influence of the contamination levels

Specified contamination levels have been established in order to achieve the $0\nu\beta\beta$ half-life target of $\sim 1 \times 10^{26}$ years for the final detector. The ^{82}Se demonstrator source is segmented in 34 foils, whose production was the responsibility of different laboratories (Dubna, LAPP and Tomsk). The sources have undergone different purification treatments, in order to investigate new techniques, and to compare them with those of NEMO-3. After the sources production and purification, preliminary measurements have been performed with the BiPo-3 detector to determine the actual ^{208}Tl and ^{214}Bi contamination levels inside the foils [19]. The level of radon emissions inside the tracker was also measured by the collaboration, for each of the four sections of the chamber, using a concentration line. We

summarise all these contamination levels in Tab. 7.2, and give a comparison with the detector initial specifications. The targeted ^{208}Tl level is not reached,

	Specified activities	Measured activities
^{208}Tl	$2\,\mu$Bq.kg^{-1}	$54\,\mu$Bq.kg^{-1}
^{214}Bi	$10\,\mu$Bq.kg^{-1}	$< 290\,\mu$Bq.kg^{-1}
^{222}Rn	0.15 mBq.m^{-3}	0.15 ± 0.02 mBq.m^{-3}

Table 7.2: Real and targeted specified activities for the SuperNEMO detector. The ^{222}Rn tracker contamination is measured with a concentration line [20], extrapolated with a 2 m^3/h flow rate. The limit on ^{214}Bi contamination is provided by BiPo measurements for a 90% CL [19].

being almost 27 times higher than expected. Nevertheless, in average, a factor of two was gained between the NEMO-3 ^{100}Mo sources and the ^{82}Se sources from the demonstrator. In addition, valuable information has been accumulated on the different production techniques, which are of great importance for the final detector construction. In particular, the two best ^{208}Tl source activities were reached by inverse chromatography, encouraging for further investigations in this direction. The sensitivity of BiPo detector only allowed to give an upper limit on the level of internal ^{214}Bi. Precise measurements are expected from the demonstrator calibration. Radon emissions from the tracker were also measured, and extrapolated with an air flow rate of 2 m^3/h inside the chamber, showing the targeted level of 0.15 mBq.m^{-3} was reached.

In Sec. 7.3, we developed the general procedure allowing to set a 90% confidence interval limit on $T_{1/2}^{0\nu}$. For the demonstrator, supposing the specified activities are reached, the demonstrator would achieve a sensitivity of 5.68×10^{24} years on the searched decay, in 2.5 years of data taking, with 7 kg of ^{82}Se. This sensitivity could be affected by the higher-than-expected level of contaminations, measured by BiPo, inside the source foils. We expose in Fig. 7.4 the $T_{1/2}^{0\nu}$ limit as a function of the contamination levels, as well as the corresponding chosen region of interest. Four distinct levels of internal contaminations are considered:

- the *zero activities* case, a hypothetical case where the source foils and the tracker are non contaminated at all,

- the *specified activities* case, were the targeted level of contaminations would have been reached,

- and two *measured* cases, that take into account the measured levels of contaminations at 90% CL. As the ^{214}Bi activity is provided by BiPo measurements as an upper limit, it is possible for this level to be lower than $290\,\mu$Bq/kg. We therefore present the results, either for sources that would not be contaminated by this isotope (the *without ^{214}Bi* case), or considering that the activity reached is $290\,\mu$Bq/kg (*with ^{214}Bi*).

The fact that we are showing results for a hypothetical zero isotope contamination is to illustrate an important statistical phenomenon. Indeed, we notice that there is
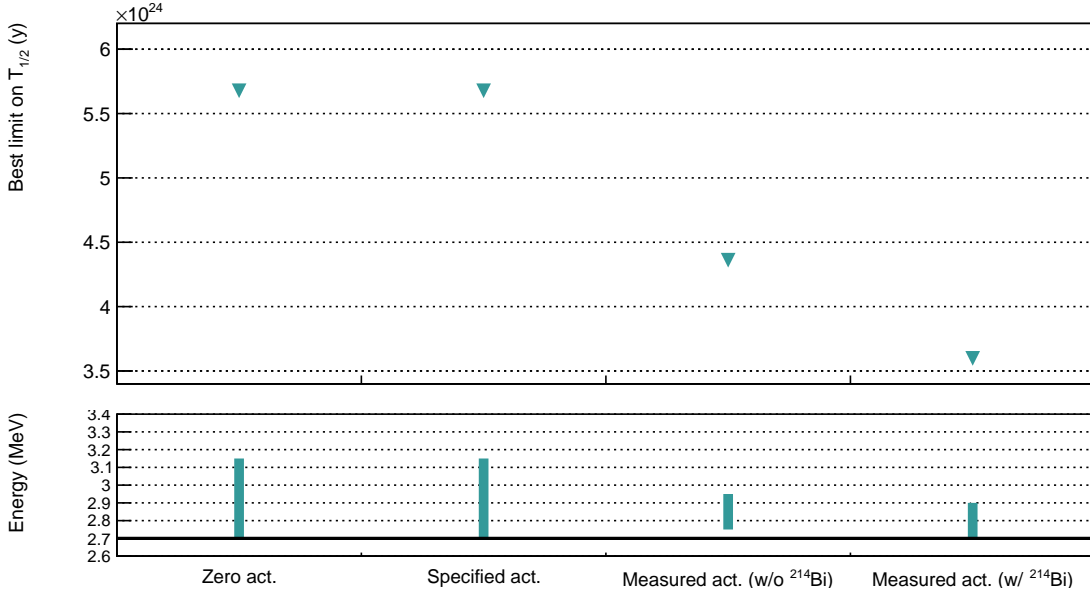
Figure 7.4: The 90% CL limit on the $0\nu\beta\beta$ half-life (top pad), and the corresponding ROI (bottom pad), as a function of the contamination level considered. For the *zero activities* case, we consider hypothetical contamination levels where $\mathcal{A}^{\mathrm{Bi}} = \mathcal{A}^{\mathrm{Tl}} = 0$ Bq/kg. The *specified activities* are presented in Tab. 7.2. The *measured activities*, provided by the BiPo detector [19], are presented in the same table. We consider successively a null ^{214}Bi contamination (*measured act. w/o ^{214}Bi*), or equals to the 290μ Bq/kg upper limit (*measured act. w/ ^{214}Bi*).

no difference in sensitivity, or ROI, between the first two cases of contamination, which may seem surprising at first glance. This is explained by the Feldman-Cousins statistics employed to determine the number of excluded signal events, $N_{0\nu}^{\mathrm{excl.}}$, given the number of observed background events (defined from Eq. (7.2) to Eq. (7.4)). When the expected number of background events is negligible (which is the case for the two first levels presented), the probability p to observe n_s signal events, expecting s events, is given by the Poisson distribution

$$p = \frac{e^{-s} s^{n_s}}{n_s!} \, . \tag{7.6}$$

Let's now put ourselves in the situation where no signal event is observed - that is what we assume to put an upper limit on the $0\nu\beta\beta$ half-life. Then $n_s \rightarrow 0$, and $p \rightarrow e^{-s}$. If zero signal event is *observed*, it is uncorrect to assume that zero signal events were *produced* during the experiment. We only can say that no signal event has been observed *a priori*. As a consequence, the quantity s is no longer the number of expected signal events, but is the number of excluded signal events, $N_{0\nu}^{\mathrm{excl.}}$. In the end, for a negligible expected number of background events, and no signal event observed, we can set an upper limit on the number of excluded signal events, excluding values for which $p < \alpha$. Taking a 90% confidence interval, that is to say $\alpha = 10\%$, we obtain $s \leq 2.303$. A direct consequence of this statement is, considering that the background levels for the two first cases are negligible (or null) in the region of interest, they both reach this limit of 2.303 on the excluded

number of signal events. Therefore, due to the Feldman-Cousins statistics, no difference is observed in terms of half-life limits between these two contamination cases.

When considering the measured internal activities, a decrease in sensitivity is observed, compared with the specified activities case. Indeed, the number of background events in the ROI is no more negligible, and influence significantly the value of $T_{1/2}^{0\nu}$, decreasing the experiment's sensitivity by 23% (without ^{214}Bi) and 37% (with ^{214}Bi). Both region of interests are also highly reduced, especially for the third contamination case, where the lower bound is greater than 2.7 MeV, an energy region populated with a non-negligible number of background events. This impacts significantly the signal-to-background ratio, and as addressed in the next subsection 7.4.2.

The degradation of the limit with the level of contamination remains acceptable. However, we can try to improve the situation by exploring new event selection techniques, with the aim of maximising the limit on $0\nu\beta\beta$ half-life.

7.4.2 Optimisation of the event selection

The measured level of ^{208}Tl isotope inside the source foils is greater than expected. Moreover, an upper limit, higher than the specified level for SuperNEMO, has been set by the BiPo detector, regarding the internal ^{214}Bi level. So we want to set up event selections, in addition to the first-order ones, adapted to each level of contamination. Most of the double beta experiments are only sensitive to the total electron energy sum. The unique SuperNEMO tracko-calo technology confers the experiment the ability to individually characterise particles (individual energies, emission angles...). By relying on these additional observables, *topological cuts* have been set up. They are especially designed to reject events where the two electrons are not emitted simultaneously, or from the same location on the source foils.

The internal probability Based on time-of-flight (TOF) computation, the internal probability (P_{int}) is derived from the internal χ^2 (see details in Sec. 4.1.1). In Fig. 7.5 are presented the internal probability spectra for the $0\nu\beta\beta$ signal and all background processes, after the first-order selections. These distributions are normalised to the double beta half-lives, and the nominal activities. Equivalent distributions, but with different ^{214}Bi and ^{208}Tl contamination levels, can be derived for the case of measured activities. The internal probability distributions for the $0\nu\beta\beta$ and $2\nu\beta\beta$ processes follow the expected flat distribution for electrons emitted simultaneously from the source. The ^{208}Tl and ^{214}Bi distributions are also flat. However, the ^{208}Tl distribution is distorted at low internal probabilities. This might be explained by the existence of a metastable excited state ($\tau_{1/2} = 294ps$) of the daughter nuclei, which would slightly delay the second electron emitted via internal conversion. This feature is addressed in detail in Chap. 8. The Radon, being a non-internal background, presents a peak at low internal probabilities.

We wish to establish the most adequate P_{int} selection level, by studying the influence of the internal probability cut-off on the final sensitivity, knowing
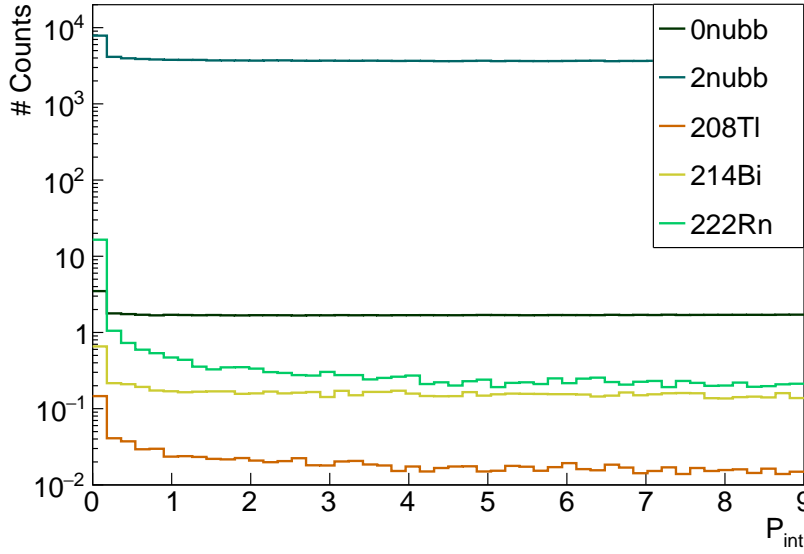
Figure 7.5: Internal probabilities for all processes. First-order cuts have been applied. $\beta\beta$ distributions are normalised to the half-lives, and background processes are normalised to the specified activities.

Eq. (7.1). To this regard, let us look at the variations in the $0\nu\beta\beta$ selection efficiency, $\epsilon_{0\nu}$, in the region of interest, as a function of the value of this cut-off (Fig. 7.6a), for the three contamination levels. In all cases, we would have expected the $\epsilon_{0\nu}$ selection efficiency to decrease with the P_{int} cut-off applied, as it is the case for the first (specified levels) and third (measured levels, with ^{214}Bi) cases. However, for the second contamination case, we observe an unusual rising of $0\nu\beta\beta$ selection efficiency. This is artificially caused by the variation of the ROI upper bound, with the P_{int} level applied. Usually, the variation of this upper bound should not have such a great impact on the event selection, as very low number of background and signal events are expected at high energies (see Fig. 7.1). However, as we can see on Fig. 7.4, the ROI chosen in that particular case is very reduced. Especially, the lower bound is located beyond the 2.7 MeV classical level. Therefore, even small variations in the ROI produces an increase of the $0\nu\beta\beta$ selection efficiency. This has a direct impact on the final sensitivity for this level of contamination. Abrupt slope changes observed for some values of P_{int}, for the cases of measured activities, are also explained by variations in the ROI limits.

As the $T_{1/2}^{0\nu}$ limit also depends on $N_{0\nu}^{excl.}$ in the ROI, we explore in Fig. 7.6b the variations of this number, obtained with the Feldman-Cousins statistics, with the set up P_{int} level. This distribution is flat for the specified level of contamination. As it was already explained in the previous subsection 7.4.1, the number of background events expected in this case is very low. In such cases, the Feldman-Cousins statistics set a minimum level of 2.303 excluded events, that are integrated over the [2.7;3.15] MeV energy range. For the case of measured internal activities, still due to variations in the ROI bounds, the excluded number of signal events vary with the P_{int} cut-off applied.
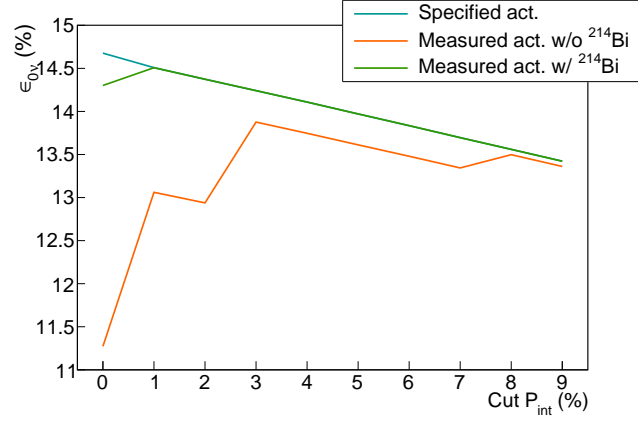
(a) $0\nu\beta\beta$ selection efficiency as a function of the cut-off applied on internal probability.
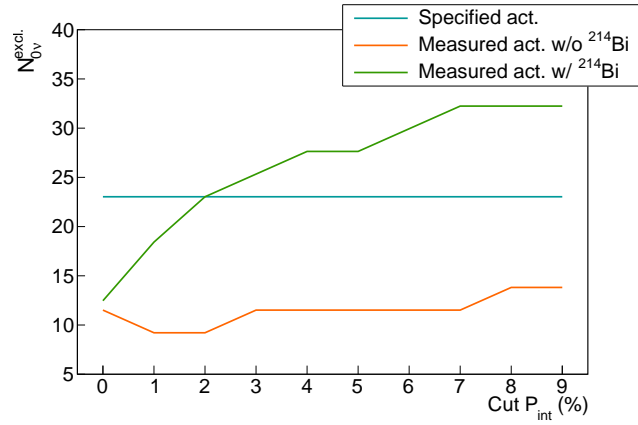
(b) Number of excluded signal events as a function of the cut-off applied on internal probability.
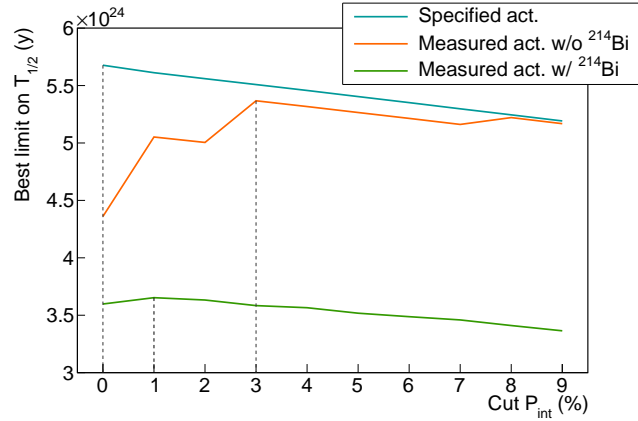
(c) Best limit set on $T_{1/2}^{0\nu}$ at 90% CL, as a function of the cut-off applied on internal probability.

Figure 7.6: Influence of P_{int} selection level on the $0\nu\beta\beta$ efficiency (a), excluded number of signal events (b) and final $T_{1/2}^{0\nu}$ limit (c), for the specified activities (blue) and the measured ones, with ^{214}Bi contamination (green) and without (orange).

As the limit set on $T_{1/2}^{0\nu}$ depends on $\epsilon_{0\nu}/N_{0\nu}^{\text{excl.}}$, the combined variations presented in Fig. 7.6a and Fig. 7.6b fully explain the results displayed in Fig. 7.6c, presenting the evolution of $T_{1/2}^{0\nu}$ with the internal probability cut. The sensitivities displayed for a 0% cut-off on P_{int} of course correspond to the results given in Fig. 7.4. We conclude that with background constraints as low as the specified activities, the internal probability cut-off only decreases the sensitivity to the $0\nu\beta\beta$ decay. Paradoxically, this selection worth it only if there is enough background events to be rejected, and we start to see the usefulness of this cut-off when we take into account the measured activities. Tab. 7.3 summarises the best internal probability cut-off to be applied in each contamination case, as well as the corresponding sensitivity achieved.

Activity	Optimised P_{int} cut-off	$T_{1/2}^{0\nu}$ (y)	
		Before cut-off	After cut-off
Specified	0%	5.68×10^{24}	$5.68 \times 10^{24}(\nearrow 0\%)$
Measured w/o ^{214}Bi	3%	4.36×10^{24}	$5.37 \times 10^{24}(\nearrow 23\%)$
Measured w/ ^{214}Bi	1%	3.59×10^{24}	$3.64 \times 10^{24}(\nearrow 1.5\%)$

Table 7.3: The optimisation of internal probability selection is presented for each background case. The corresponding limit on $T_{1/2}^{0\nu}$ at 90% level, before and after the P_{int} cut-off, is given.

Vertices distance As discussed in Sec. 7.2, an electron is defined as a reconstructed track inside the wire chamber, with one vertex on a calorimeter block, and another on a source foil. Therefore, the $2e$ topology involves two distinct calorimeter vertices, two resonstructed tracks, and two foil vertices. Thanks to the trajectory fitting algorithm, we have access to the (Y, Z) coordinates of the latter, and by extension, to the distance between them. In the previous studies that have been conducted, the choice was made to look at the effect of a selection on distance between vertices, separately on the Y (perpendicular to the wires) and Z (paralel to the wires) directions. We choose to follow the same approach, and we give the results for a cut along the Z axis, but the conclusions remain valid for the Y direction. Fig. 7.7 shows the distributions of the distance between foil vertices for each process studied. We would use this information in order to maximise the double β decays to be selected, while rejecting natural isotope disintegrations.

Fig. 7.8 displays the limit set on $T_{1/2}^{0\nu}$ as a function of this event selection, allowing to study the impact of the vertices distance cut-off on the final sensitivity. The three distributions reach a plateau, corresponding to the maximum $T_{1/2}^{0\nu}$ that can be achieved with the cut-off, already applied, in internal probability. Regardless of the level of contamination, the cut-off only degrades the results. As we said, before applying the ΔZ selection, the P_{int} optimised cut-off had already been applied. The number of remaining background events is too low for the ΔZ cut-off to be worthwhile. The same conclusions apply to the ΔY cut-off.

The idea of having implemented these two selections (on the internal probability and on the distance between vertices) comes from a previous NEMO-3 analysis on
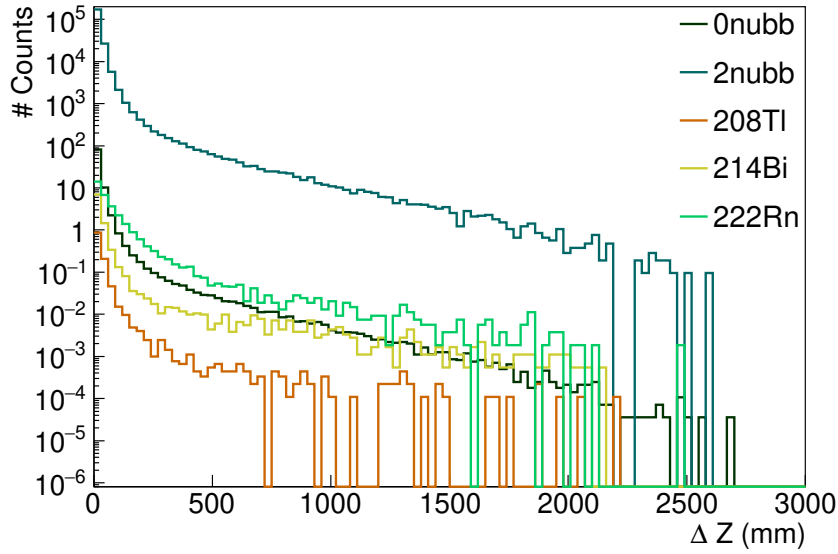
Figure 7.7: Distance between vertices along the Z direction, for each process considered.

the background rejection. However, the levels of contaminations we are dealing with is remarkably low for most of the the topological cut-offs to be worth applying. After looking at the effect of contaminations on the sensitivity, we review the influence of the magnetic field inside the detector.

7.5 Impact of the magnetic field on the sensitivity

The SuperNEMO demonstrator was originally designed with a copper coil, similarly to NEMO-3, delivering a magnetic field inside the tracker volume, aiming to provide an electron/positron discrimination. This 25 G magnetic field is high enough to bend the trajectory of the few MeV electrons and positrons of interest for SuperNEMO, without preventing them from reaching the calorimeter. In practice, this magnetic field is mainly used to identify and reject the electron-positron pairs created by high energy γ's, themselves emitted after a neutron capture. In this study, however, we choose to not consider the contribution of this external background. We therefore focus on evaluating the influence of the presence of the magnetic field on the rejection of internal and wire chamber backgrounds.

7.5.1 Simulations of the magnetic field inside the demonstrator and reconstructed track fit

In order to study the influence of the magnetic field on the Selenium-82 $0\nu\beta\beta$ sensitivity, the simulations and reconstructions of decays described in Sec. 7.1 have been performed in two different conditions.
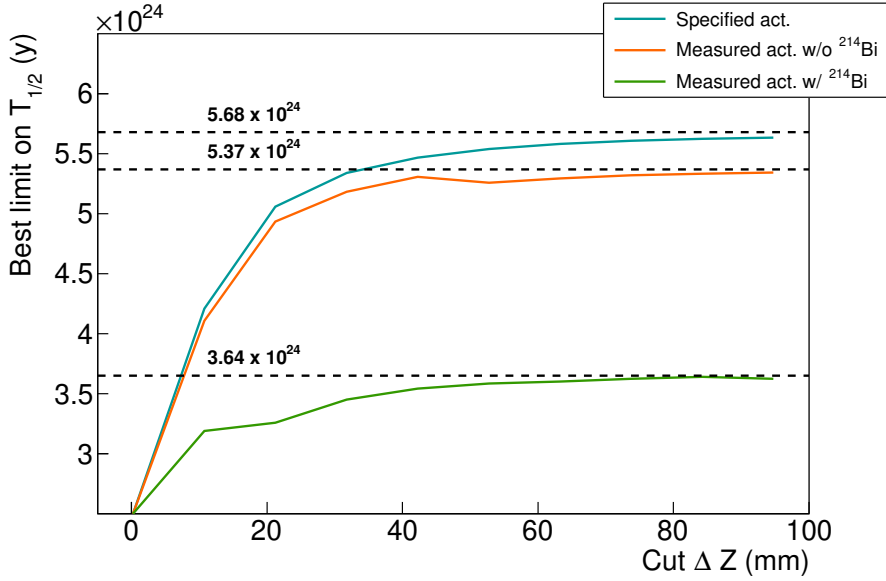
Figure 7.8: Best reached limit on $T_{1/2}^{0\nu}$, as a function of the cut-off applied on the Z distance between vertices. Results are displayed for specified (blue), and measured contaminations (with the ^{214}Bi contamination (orange) or without it (green)). No improvement in sensitivity is obtained with this event selection.

- Simulations with a 25 G magnetic field (following recommendations [9]). Results about the final sensitivity achieve have already been presented earlier in this chapter. The possible variations of the field intensity, mainly due to possible interferences with the detector materials, are not taken into account for these simulations. This will be discussed in subsection 7.5.4.

- Simulations where the magnetic field is turned off.

Each magnetic field condition has the same number of simulated events, as summed up in Tab. 7.1. Depending on the case considered, the electrons do not have the same trajectory curvature. In the first uniform on-field case, the best track fit is performed by helices. In the second off-field case, the motion of an electron is in a straight line. The fitting algorithm have thus be modified to match line trajectories.

We oppose in Fig. 7.4 the $T_{1/2}^{0\nu}$ results with and without this field inside the detector.

7.5.2 Impact of the magnetic field on signal background selections

Among the various event selection criteria considered in Sec. 7.2, the last one is of primary importance with regard to the influence of the magnetic field on the final sensitivity of the detector. Indeed, when the magnetic field is switched on, the charged particles of few MeV (as electrons and positrons) have a curved trajectories. A particle is then identified as an electron when the trajectory

fitting results in a negative curvature. When the magnetic field is switched off, the trajectory of the charged particles takes place in a straight line[3]. This last selection criterion is then no longer applied. Consequently, the number of identified $2e$ topologies, selected by the first-order cuts, are increased, for the signal and background simulated events. To illustrate this effect, we give in Fig. 7.9 the selection efficiency $\epsilon_{0\nu}$ as a function of the $2e$ total energy, for the two cases of magnetic field presented above. The two coloured stripes represent
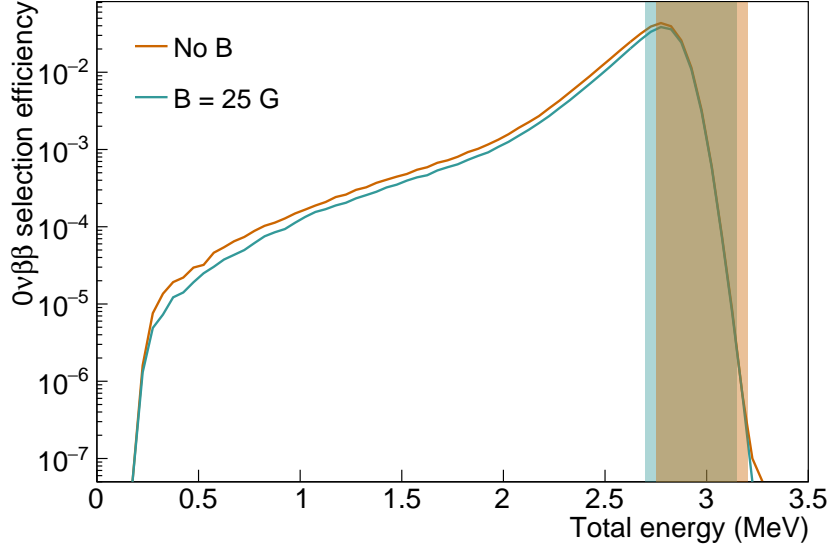

Figure 7.9: The $0\nu\beta\beta$ selection efficiency as a function of the $2e$ total energy, for the on-field (blue) and the off-field (orange) cases. The two corresponding region of interests are also displayed by coloured stripes. Here no optimised topological cut-offs have been applied.

the corresponding region of interests, of [2.7;3.15] MeV for the *on-field* case, and [2.75;3.2] MeV for the *off-field* case. These results are presented for the specified contamination levels, but remain valid in all cases. We clearly notice that, for the total energy interval [0;4] MeV, the number of $0\nu\beta\beta$ events selected is higher in the off-field case, which confirms what we were saying above.

The $0\nu\beta\beta$ selection efficiency in the region of interest directly impacts the final sensitivity, following Eq. (7.1). Indeed, the upper limit set on $T_{1/2}^{0\nu}$ depends on $\epsilon_{0\nu}$ as well as on $N_{0\nu}^{\text{excl.}}$, the number of signal events excluded. Nevertheless, for such levels of contaminations, due to the Feldman-Cousins statistics, the latter has no effect on sensitivity, and only the $0\nu\beta\beta$ selection efficiency in the region of interest plays a role. For the two field cases of interest, these efficiencies are $\epsilon_{0\nu}^{\text{on-field}} = 0.15\% > \epsilon_{0\nu}^{\text{off-field}} = 0.12\%$. The selection efficiency for the on-field case is favoured by the lower bound of the ROI. In fact, the further this lower bound is shifted towards lower energies, the greater the selection efficiency. Besides, slight variations of the upper bound have almost no impact. As expected, this results in

---

[3]When we say this, we do not take into account possible deviations in the trajectory of the particles, due in particular to multiple scattering in the tracker.

a decrease in sensitivity for the off-field case, giving

$$T_{1/2}^{0\nu} > 4.80 \times 10^{24}\,\text{y} \qquad (90\%\text{CL})\,. \qquad (7.7)$$

However, this decrease in sensitivity when the field is switched off can be compensated by applying the topological cut-offs described in subsection 7.4.2. We optimised these selections for each contamination level case, and for both field and no field cases. In Fig. 7.10 are presented the best values for $T_{1/2}^{0\nu}$, using optimised topological cut-offs, both for on-field (see Tab. 7.3) and off-field cases. The topological cuts allow to increase the final sensitivity. The $T_{1/2}^{0\nu}$ value for off-
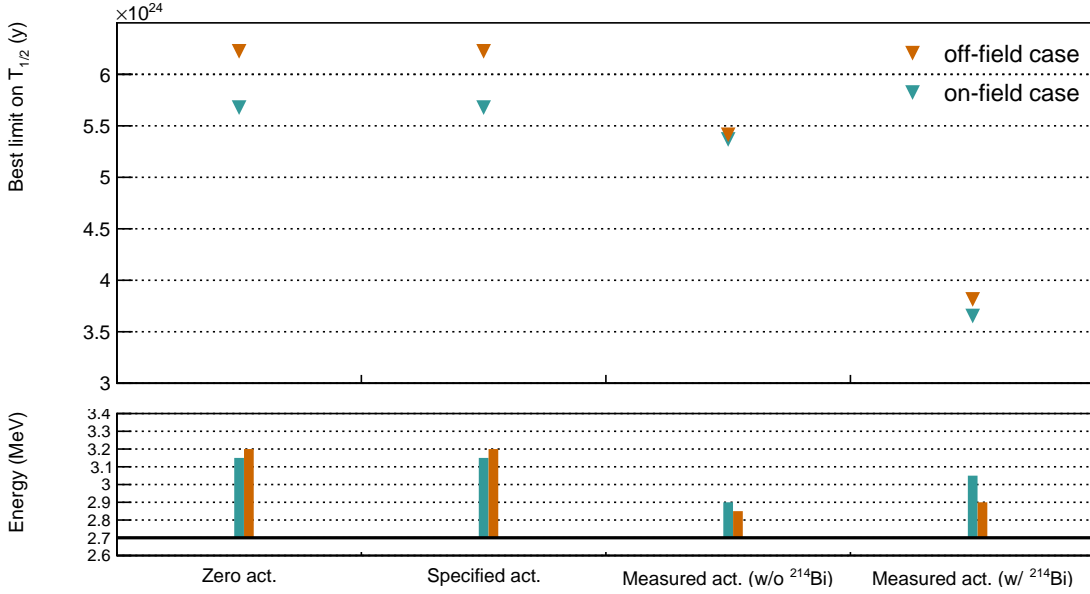
Figure 7.10: Best limit set on $0\nu\beta\beta$ half-life (top pad), and the corresponding ROI (bottom pad), as a function of the contamination level considered, for both on-field and off-field cases.

field case, taking the specified activities, goes from 4.80×10^{24} y to 6.22×10^{24} y, an improvement of 30%. Because of the higher level of selected $2e$ topologies, higher sensitivities can be reached for the off-field case than for the on-field case, if using optimised topological cut-offs. More generally, by using first-order cuts as well as topological cuts adapted to each case, we achieve higher sensitivities for the off-field case. We note, however, that for high contamination levels (i.e. measured activities with and without bismuth), the difference in sensitivity for the two magnetic field cases tends to decrease.

7.5.3 Influence of the magnetic field on optical modules and reconstruction efficiency

Studies have been lead to evaluate its influence on the optical modules and on the event reconstruction [9][17].

SuperNEMO PMTs are protected from the external magnetic field by an iron shield. Unfortunately, the latter do not perfectly protect the PMTs, and

a residual magnetic field is measured inside the shieldings, leading to charge losses and worsened energy resolution. It was shown that applying a 25 G magnetic field, and protect the PMTs with iron magnetic shields would be optimal, but not without consequences. In fact, for the recommended value of 25 G for the magnetic field, PMT charge losses would be close to 8%, and the PMT energy resolution would be increased of $\sim 3\%$. Moreover, the PMTs shieldings could themselves severely impact the shape of the field lines, as well as its strength. In fact, with a 25 G magnetic field generated by the copper coil, the magnetic shields are responsible for the field strength decreasing, and barely 10 G is expected near the source foils. Moreover, the magnetic field strength decreases quickly as we get closer to the calorimeter walls. The reconstruction efficiency could therefore be greatly impacted: the magnetic field intensity varying from the source foils to the calorimeter wall, electrons trajectory curvatures are not constant, and the track is less well fitted. This effect is higher as the electron energy decreases.

Despite the fact that magnetic shields were designed and installed to protect the PMTs, this field can have a great impact on the calorimeter detection efficiency, and thus could degrade the detector's sensitivity to the $0\nu\beta\beta$ decay. If the studies cited have evaluated the influence of the presence of the magnetic field on the reconstruction efficiency of $0\nu\beta\beta$ events, it remains to be seen its consequences on the final demonstrator sensitivity.

7.5.4   Simulations with a more realistic magnetic field

7.6   Searching for the Neodymium-150 $0\nu\beta\beta$ decay

This study was conducted jointly with the PhD student Axel Pin, from CENBG []. Although we both worked on the whole of the analysis, I presented in detail, in the previous sections, the results regarding the influence of the magnetic field. Meanwhile, Axel Pin present in detail the possibility of changing the Selenium material by Neodymium sources [21]. The current section aims at summarise the feasibility study on Neodymium sources.

In the case SuperNEMO demonstrates the feasibility of a large-scale tracko-calo experiment, we would examine the possibility of different source isotopes, as done on NEMO-3. The ^{150}Nd has a more favourable $Q_{\beta\beta}$ than ^{82}Se, with $Q_{\beta\beta} = 3.37$ MeV, . However, its $T_{1/2}^{2\nu}$ is lower, with 9.1×10^{18} years [ref]. For this study, we keep the ^{82}Se values for the contaminations, despite different purification efficiencies for the two isotopes.

- préciser que compte-tenu du Z important du 150Nd, même si la demi-vie de la 2nu est assez faible, cela ne gêne pas trop car les effets coulombiens font que la 2nu ne contribue pas trop à haute énergie.

- distribution t1/2 avec différents échantillons de simus (17.5 kg.y)

7.7   The final detector sensitivity

The final goal of the SuperNEMO demonstrator is to demonstrate that the NEMO technology is scalable to reach high half-life sensitivity on the $0\nu\beta\beta$ decay. It was therefore mandatory to study the case of the final detector sensitivity, consisting in building 20 modules similar to the SuperNEMO demonstrator, to reach unprecedented levels on effective neutrino masses.

7.8   Conclusion

- Etude plus générale avec bkg externe+lab (reprendre chiffres NEMO3) + neutrons (cf NEMO3)

- Plot général récap tous résultats

- delayed cells-¿improvement, cf NEMO 3

- ouverture sur possibilité d'étudier l'influence de la résolution en temps des PMs sur l'eff des coupures (Pint)

- cellules tracker dead-¿ refaire analyse

- manque de stat pour le neodyme car ROI haute E

- légères diff avec résultats axel car légères diff dans sélections d'ev car utilisation PID

- tenir compte de la dégradation en énergie dans les simus du au B

- optimisation topo cuts : multivariate analysis peut être envisagée pour aller plus loin

- ajouter possibilité champ mappé

Bibliography

[1] M. et al. Agostini. Probing majorana neutrinos with double-β decay. *Science 365*, 1445, 2019.

[2] S.I. et al Alvis. Search for neutrinoless double-beta decay in ^{76}ge with 26 kg-yr of exposure from the majorana demonstrator. *Phys. Rev. C*, 100, 2019.

[3] O. et al. Azzolini. First result on the neutrinoless double-β decay of ^{82}Se with cupid-0. *Phys. Rev. Lett.*, 120:232502, Jun 2018.

[4] C. et al. Alduino. First results from cuore: A search for lepton number violation via $0\nu\beta\beta$ decay of ^{130}Te. *Phys. Rev. Lett.*, 120:132501, Mar 2018.

[5] J. B. et al. Albert. Search for neutrinoless double-beta decay with the upgraded exo-200 detector. *Phys. Rev. Lett.*, 120:072701, Feb 2018.

[6] A. et al. Gando. Search for majorana neutrinos near the inverted mass hierarchy region with kamland-zen. *Phys. Rev. Lett.*, 117:082503, Aug 2016.

[7] Nucleid database.

[8] R. et al. Arnold. Probing new physics models of neutrinoless double beta decay with supernemo. *Eur. Phys. J. C*, 2010.

[9] S. Clavez. *Development of reconstruction tools and sensitivity of the SuperNEMO demonstrator*. PhD thesis, Université Paris Sud, 2017.

[10] Gomez-Cadenas et al. Physics case of supernemo with ^{82}se source. Internal presentation, 2008.

[11] R. et al. Arnold. Final results on ^{82}se double beta decay to the ground state of ^{82}kr from the nemo-3 experiment. *Eur. Phys. J. C*, 2018.

[12] Tretyak V.I. Ponkratenko O.A. and Zdesenko Yu.G. The event generator decay4 for simulation of doublebeta processes and decay of radioactive nuclei. *Phys. At. Nucl.*, 63:1282–1287, Jul 2000.

[13] Perrot F. Radiopurity measurements for 8" pmts and preliminary budget for the sn demonstrator. Internal presentation, 2017.

[14] R. et al. Arnold. Results of the search for neutrinoless double-β decay in ^{100}mo with the nemo-3 experiment. *Phys. Rev. D*, 2015.

[15] Steven Calvez. Updates on the demonstrator sensitivity and radon study. Internal presentation, 2014.

[16] Cousins D. Feldman G. A unified approach to the classical statistical analysis of small signals. *Phys.Rev.*, pages 3873–3889, 1999.

[17] Garrido X. Bongrand M. Hamamatsu 8" pmt test in magnetic shield. Internal presentation, 2014.

[18] Snow S. A magnetic field map for the tracker. Internal presentation, 2015.

[19] Loaiza P. Source foils measurement with bipo. Internal presentation, 2017.

[20] Xin Ran Liu. Radon mitigation strategy and results for the supernemo experiment. IoP APP / HEPP Conference, 2018.

[21] A. Pin. *Recherche de la nature du neutrino via la décroissance double bêta sans émission de neutrinos. Caractérisation et optimisation du calorimètre SuperNEMO et impact sur la recherche de la décroissance du 82Se Développement du premier prototype LiquidO.* PhD thesis, Université Bordeaux-Gradignan, 2020.